

Evaluating radiation impact on transmon qubits in above and underground facilities

Francesco De Dominicis,^{1,2,*} Tanay Roy ^{*,3,†} Ambra Mariani,^{4,‡} Mustafa Bal,³ Nicola Casali,⁴
 Ivan Colantoni,⁴ Francesco Crisa,⁵ Angelo Cruciani,⁴ Fernando Ferroni,^{1,4} Dounia L Helis,²
 Lorenzo Pagnanini,^{1,2} Valerio Pettinacci,⁴ Roman M Pilipenko,³ Stefano Pirro,² Andrei Puiu,²
 Alexander Romanenko,³ David v Zanten,³ Shaojiang Zhu,³ Anna Grassellino,³ and Laura Cardani⁴

¹*Gran Sasso Science Institute*

²*INFN, Laboratori Nazionali del Gran Sasso*

³*Superconducting Quantum Materials and Systems Division,
 Fermi National Accelerator Laboratory (FNAL), Batavia, IL 60510, USA*

⁴*INFN, Sezione di Roma*

⁵*Illinois Institute of Technology*

(Dated: May 29, 2024)

Superconducting qubits can be sensitive to abrupt energy deposits caused by cosmic rays and ambient radioactivity. Previous studies have focused on understanding possible correlated effects over time and distance due to cosmic rays. In this study, for the first time, we directly compare the response of a transmon qubit measured initially at the Fermilab SQMS above-ground facilities and then at the deep underground Gran Sasso Laboratory (INFN-LNGS, Italy). We observe same average qubit lifetime T_1 of roughly 80 microseconds at above and underground facilities. We then apply a fast decay detection protocol and investigate the time structure, sensitivity and relative rates of triggered events due to radiation versus intrinsic noise, comparing above and underground performance of several high-coherence qubits. Using gamma sources of variable activity we calibrate the response of the qubit to different levels of radiation in an environment with minimal background radiation. Results indicate that qubits respond to a strong gamma source and it is possible to detect particle impacts. However, when comparing above and underground results, we do not observe a difference in radiation induced-like events for these sapphire and niobium-based transmon qubits. We conclude that the majority of these events are not radiation related and to be attributed to other noise sources which by far dominate single qubit errors in modern transmon qubits.

In recent decades, superconducting circuits have emerged as a leading technology explored in the fields of quantum information [1–6], photon and particle detectors [7–16]. In the past years, several research groups have started investigating the effect of particle interactions on the performance of quantum bits (qubits) [17, 18]. There are many studies investigating these potential effects in superconducting quantum devices of various geometries and materials. Some early work pointed to the lifetime of a transmon qubit potentially decreasing when exposed to a strong radioactive source [19]. Moreover, the effect of high energy deposits can rapidly propagate from the initial location of deposition, affecting multiple qubits and potentially leading to a general chip failure [20, 21]. C.D. Wilen et al.[22] observed that the rate of charge jumps experienced by an array of qubits (operated as electrometers) was consistent with the rate expected from interactions due to ambient radioactivity and cosmic rays. Thorbeck et al. [23] did not observe significant radiation effects, but concluded that the impacts due to radioactivity may induce frequency jumps in a dominant loss mechanism, namely two-level systems (TLS) [24–31], possibly affecting qubit stability.

Other studies have shown that suppressing radioactiv-

ity can enhance the performance of superconducting circuits. Operating the device in a radio-pure facility has allowed to significantly improve the locking of a fluxonium qubit at the sweet spot [32] and enhanced the internal quality factor of superconducting resonators [33]. The latter publication also enabled the determination that the substrate on which qubits are deposited, rather than the qubits themselves, is the primary target for particle interactions.

These findings have motivated efforts in further directions aimed at studying and mitigating possible effects of radioactivity. Promising results have been achieved by equipping the chip with “traps” designed to absorb phonons produced (also) by radioactive interactions [34–36] and using gap engineering [18]. Some groups are also focusing on the components used to construct and operate qubits [37, 38], as it has been demonstrated that some of them, such as the Printed Circuit Boards (PCBs), can produce a sizeable rate of events in the qubit chip [39]. Furthermore, it is also worth mentioning recent proposals of equipping qubits with a device specialised in recognizing particle interactions [40] or with external muon detectors [21, 41, 42].

In this work, for the first time, we study charge-insensitive transmon qubit devices in two laboratories with very distinct radiation environments, as a step of the Superconducting Quantum Materials and Systems (SQMS) Center *Round Robin* project [39], which aims at studying identical qubits measured at multiple test sites

* Equal contribution

† Corresponding author: roytanay@fnal.gov

‡ Corresponding author: ambra.mariani@roma1.infn.it

around the world. We first compare average relaxation times measured over several hours, and then employ a fast decay detection protocol to identify reductions in relaxation time at rates faster than 10 kHz and analyze time-bin correlations to determine the characteristics of the events. We study the response of the qubit in a controlled environment, by exposing it to gamma-ray sources of increasing activity. Using the same protocol and analysis strategy, we investigate similar qubits hosted above ground in a typical laboratory environment, to compare effect of radiation on transmon qubits performance and behavior, and estimate timescales at which radiation may become concerning for quantum computational errors.

I. EXPERIMENTAL LOCATIONS

To perform the comparative study, we operated similar transmon chips (charge-insensitive) in two different laboratories: the *Quantum Garage* of the SQMS Center at Fermilab (FNAL, Illinois, US), and the *Ieti Facility* located in the deep underground Gran Sasso Laboratory of INFN (INFN-LNGS, L'Aquila, Italy). The chip consisted of a $432\ \mu\text{m}$ thick, $7.5 \times 7.5\ \text{mm}^2$ wide HEMEX grade Sapphire substrate. Eight Niobium transmons with different geometries were deposited on the chip (see Supplementary section A); their surface was capped using a $\sim 10\ \text{nm}$ thick layer of Gold (measured at both sites) or Tantalum (measured at FNAL) to reduce losses due to the formation of Nb_2O_5 [43]. The capping technique allowed to achieve excellent T_1 of many tens and up to hundreds of microseconds, which is important to study the change in qubit's lifetime at microsecond timescales.

We characterized several qubits of these chips operated at FNAL and at INFN-LNGS, and performed comparisons for either an identical qubit or qubits of similar geometries and materials employed. The detailed parameters of these devices are provided in the Supplementary Section A. Additionally, it is noteworthy that the entire substrate is covered in Niobium creating a ground plane; this may act as a phonon trap, diminishing the phonon propagation and absorption in the active part of the qubit [44, 45].

To predict the rate of impacts due to ambient radiation, we conducted a Monte Carlo simulation using the GEANT4 framework [46] developed in Ref. [39]. We anticipate the total rate of radioactive events interacting with the chip at FNAL and INFN-LNGS to be $(57 \pm 3) \times 10^{-3}$ events/sec and $(4.0 \pm 0.6) \times 10^{-3}$ events/sec, respectively. Table I provides a summary of the simulation results, with detailed information provided in the Supplementary Section C.

At FNAL (see Fig. 1(a)), the rate is primarily dominated by γ rays produced by the decay of naturally radioactive isotopes present in the laboratory environment. However, muons generated by cosmic rays also contribute significantly to the overall rate. In contrast, at INFN-LNGS (see Fig. 1(a)), muons are suppressed by

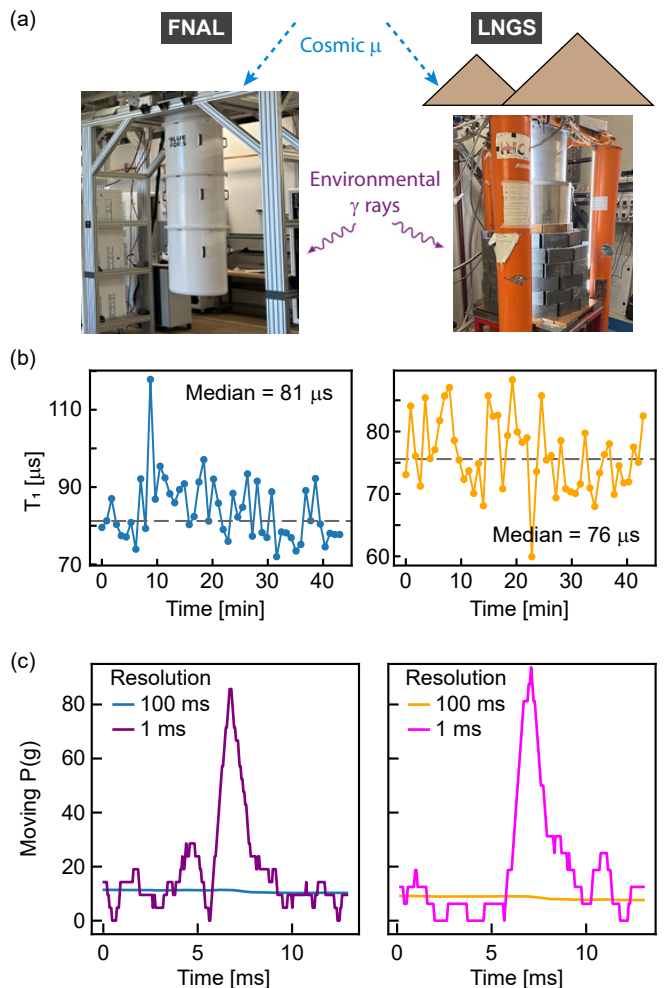


FIG. 1. **Comparison of two experimental sites.** (a) The above-ground cryostat at FNAL is not actively protected from any radiation, whereas, the deep-underground one at LNGS is strongly guarded from cosmic muons by the 1.4 km deep rock and from environmental γ rays through a ten cm thick lead shield. The left and right panels present data taken at FNAL and at LNGS respectively. (b) Standard T_1 measurements performed on the same device for a long period show similar fluctuations. These measurements are slow (takes seconds) and cannot capture the T_1 drops that persist at millisecond time scales potentially due to radiation impact. (c) The graphs display the moving probability of detecting in $|g\rangle$ with 1 ms and 100 ms time resolution (see Fig. 2(c)). The features (purple and pink traces) corresponding to low T_1 periods obtained with 1 ms resolution at two laboratory locations show very similar profile. The low resolution traces (blue and orange) clearly show that an event will go undetected and thus cannot be observed with regular T_1 experiments due to its averaging nature.

six orders of magnitude thanks to the 1.4 km thick rock overburden. Moreover, the radioactivity of the laboratory is substantially reduced by copper and lead shields positioned both inside and around the refrigerator. The last source of radioactivity arises from the materials constituting the qubit chip and its nearby readout compo-

Source	FNAL [events/sec]	INFN-LNGS [events/sec]
Lab γ -rays	$(46 \pm 2) \times 10^{-3}$	$(1.3 \pm 0.1) \times 10^{-3}$
Muons	$(8 \pm 0.5) \times 10^{-3}$	$< 10^{-5}$
Setup	$(2.7 \pm 0.5) \times 10^{-3}$	$(2.7 \pm 0.5) \times 10^{-3}$
Total	$(57 \pm 3) \times 10^{-3}$	$(4.0 \pm 0.6) \times 10^{-3}$

TABLE I. **Simulated rate of interactions in the Sapphire substrate.** For the computation of the FNAL rates, we assumed a “standard” γ -ray flux of $(2.5 \pm 0.5) \gamma/\text{cm}^2/\text{sec}$ and a muon flux of $1 \mu/\text{cm}^2/\text{min}$. For INFN-LNGS, we measured a flux of $(1.0 \pm 0.5) \gamma/\text{cm}^2/\text{sec}$; the suppression factor due to the presence of lead and copper shields was evaluated through a Monte Carlo simulation. Finally, the radioactive contamination of the components of the setup was measured in Ref. [39].

nents. In a previous study conducted within the SQMS *Round Robin* project [39], we measured the radioactive content of each component and determined that cables, connectors, amplifiers, circulators, etc., have a negligible impact on the total event rate. The only exception is the PCB, which is typically highly contaminated and located in close proximity to the chip. In this setup, the PCBs are responsible for the whole counting rate reported in the line “Setup” of Table I. While this rate is negligible at FNAL, it becomes the dominant source of radioactivity at INFN-LNGS, where all external sources of radioactivity are suppressed.

Furthermore, at INFN-LNGS, we utilize Thorium radioactive sources to increase the event rate up to one event every two seconds and investigate the chip behaviour in a “high”-radiation environment.

II. EFFECT OF RADIATION IMPACT

When a radioactive particle impinges on the qubit chip, it releases energy. Muons create long tracks across the chip, whereas γ rays interact through photo-electric absorption or (mainly via) Compton scattering, producing short-track electrons. In the absence of an electric field, the thousands of charges created along the ionizing track recombine into phonons, which diffuse throughout the chip [22]. As illustrated in Fig. 2(a), when phonons interact with a superconductor, they can break Cooper pairs into quasiparticles. Subsequently, when one or more quasiparticles tunnel through the Josephson Junction, the qubit loses its energy and quickly decays to its ground state $|g\rangle$ [35] with a timescale of 0.16-1.6 μs [47, 48]. Since the metallic pads of the transmon host a large number of quasiparticles that take some time to dissipate through normal metal (PCB leads) or lower-energy phonon scattering, these tunneling events can continue to occur, causing the qubit to suffer from strong relaxation for some time. Previous studies claim this low T_1 periods to last from one to several tens of milli-seconds [20, 21]. We investigated these type of events in our studies.

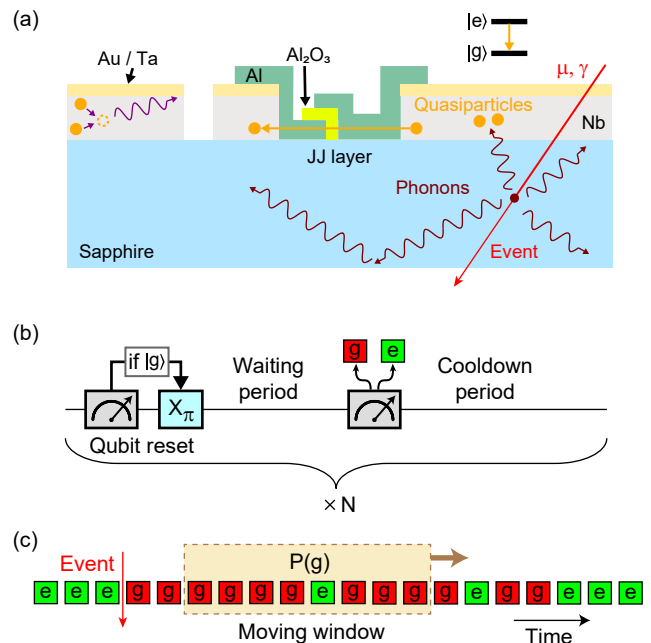


FIG. 2. **Quasiparticle generation process and experimental protocol.** (a) Sketch of the quasiparticles generation process due to particle interactions in the substrate. Ionizing radiation impinging on the substrate produces electron-hole pairs, which recombine creating phonons. These phonons spread throughout the chip and, in superconducting structures, can break Cooper pairs into quasiparticles, which can tunnel across the Josephson Junction inducing decay of the qubit from the excited state $|e\rangle$ to the ground state $|g\rangle$. (b) The fast decay detection protocol consists of repeated cycles of preparation in the excited state, waiting period, measurement and cooldown periods. The duration of each cycle is less than 90 μs , while the waiting time is 5 μs . (c) During normal periods the qubit is highly likely to be found in the excited state due to long T_1 . An event causes a drastic reduction in qubit’s lifetime resulting in repeated detection in $|g\rangle$ and hence increasing the probability $P(g)$ of finding the qubit in $|g\rangle$ given a suitably chosen time window. The qubit gradually recovers its natural T_1 . The measured sequence is analyzed to detect radiation impacts with sub-milli-second resolution

We first performed standard T_1 experiments on both underground and above ground locations on the identical qubit Q1 and monitored the relaxation times for close to an hour. These experiments were slow and each data point took about 50 seconds to complete. The results, plotted in Fig. 1(b), show similar mean values and fluctuations, typical for transmon qubits [43], demonstrating that radiation has no significant effect at current state-of-the-art transmon qubit lifetimes of 100 microseconds. No sudden drop in T_1 values was observed. This was expected as the standard T_1 experiments, due to its averaging nature, are not sensitive to fluctuations at milli-second timescales. In order to study possible events at such a time resolution we employed a protocol, tailored for single qubits, utilizing fast decay measure-

ments [18, 20].

Datasets	acquisition time	live-time
	[min]	[min]
Shielded chip	676.0	28.2
Shielded chip (2)	–	124.0
44 kBq Th Source	619.5	114.0
76 kBq Th Source	111.7	46.3
125 kBq Th Source	60.9	28.2
161 kBq Th Source	60.9	54.3
FNAL Q2	234.5	104.0
FNAL Q3	449.7	141.9
FNAL Q4	242.7	25.9

TABLE II. **List of datasets.** Top rows correspond to data taken at LNGS using Q1. The original duration (acquisition time) and ‘live-time’ duration after removing period of time where the second excited state $|f\rangle$ is highly populated. To increase the statistics of the shielded chip, we used also a second Dataset where $|f\rangle$ was partially excited. Datasets taken at FNAL correspond to measurements on three different qubits.

The fast detection protocol illustrated in Fig. 2(b) begins by resetting the qubit in its excited state $|e\rangle$. This is accomplished by initially measuring the qubit and applying a conditional π -pulse if the qubit is found to be in state $|g\rangle$ via fast feedback. Following a waiting period Δt_d lasting a few microseconds, the qubit is measured again to determine whether it is in state $|g\rangle$ or $|e\rangle$. Given a sufficiently long qubit T_1 , the qubit is highly likely to be found in state $|e\rangle$. Theoretically, the qubit relaxes to state $|g\rangle$ only a small fraction of the time, given by $(1 - e^{-\Delta t_d/T_1}) \approx \Delta t_d/T_1$. However, a radiation event significantly reduces the T_1 , making it highly probable for the qubit to be detected in state $|g\rangle$. The sequence is then repeated after another short period, allowing the chip to cool down. Since the effect of quasiparticle generation persists longer than the time taken for one sequence, an event due to radiation typically results in repeated detection in state $|g\rangle$, as depicted in Fig. 2(c).

In our measurements, we kept the waiting period fixed to 5 μs while other parameters like π -pulse and readout pulse lengths were similar and reported in the Supplementary Section A. The cooldown period is chosen to ensure that the transmon does not exhibit excessive population in the second excited state $|f\rangle$. Nevertheless, a simultaneous fit of the $|g\rangle$, $|e\rangle$ and the second excited state $|f\rangle$ showed that there were many moments in which the $|f\rangle$ (and sometimes even the third excited state $|h\rangle$) states were populated. To ensure data consistency, we excluded these time intervals. A thorough investigation of this phenomenon will be mandatory for applications in sensing, as this selection significantly limits the measurement’s live-time (see Table II).

The readout scheme employed is detailed in the Supplementary Section B. The input signal, filtered through attenuators, low-pass filters, and infrared filters, is sent

to the qubit; the output signal is fed into cryogenic triple-junction isolators, and then amplified via a cryogenic HEMT followed by a room temperature amplifier. The qubit readout and control are performed through an RF-SoC board using the Quantum Instrumentation Control Kit (QICK) [49]. Each measurement generates a complex number (I/Q values) that are post-processed to distinguish between $|g\rangle$ and $|e\rangle$ based on readout calibration.

We acquired the data for several hours containing several hundred million readouts. During the initial analysis, we simply computed the probability $P(g)$ of finding a qubit in $|g\rangle$ for a fixed time window and plot $P(g)$ as we moved the window (see Fig. 2(c)). A typical record of $P(g)$ as a function of time is shown in Fig. 3(a). The magenta color is the mean of the trace while the fluctuations in the trace look steady. A clear spike around 18.2 seconds corresponds to an event with drastic T_1 drop. When zoomed in, these spikes show different pulse shapes as plotted in Fig. 3(b). These pulses generally have a sharp rise but the fall times vary between different instances. As depicted in Fig. 1(b), we found pulses of similar time-profile at both locations irrespective of the specific qubit, pointing to the fact that the drop in relaxation time is not tied to a specific transmon. All pulses observed in our studies last less than ten milliseconds in agreement with the study in Ref. 21 and thus these pulses require multiple qubit measurements within a milli-second for being detected. For example, the pulses in Fig. 1(c) are visible when a one ms time-window is selected for computing $P(g)$ and the signal vanishes when a course time-window of 100 ms is chosen. Clearly, a slow measurement scheme will not be able to resolve individual radiation impact events. In other words, standard T_1 measurements, due to its slow nature, will not be affected by radiation impacts (happening at intervals of several seconds) as demonstrated earlier.

A simple detection strategy based on triggering pulses on the $P(g)$ data by setting a constant threshold, however, suffers from the problem that a large threshold misses many events, whereas, a lower value picks up a lot of noise arising inherently from the qubit measurement. Furthermore, such a noise is not stable in time leading to unexpected variations when setting a simple constant threshold. As shown in Fig. 3(c), the $P(g)$ traces occasionally show noisy behavior which do not follow any adjacent spike. These periods of instability can last from sub-seconds to a minute and will affect regular T_1 experiments. Even though it appears to be related to TLS scrambling, we currently do not have a clear understanding of the source of this behavior and it will be a subject of future studies. Consequently, to improve the detection efficiency, we develop a modified strategy discussed below.

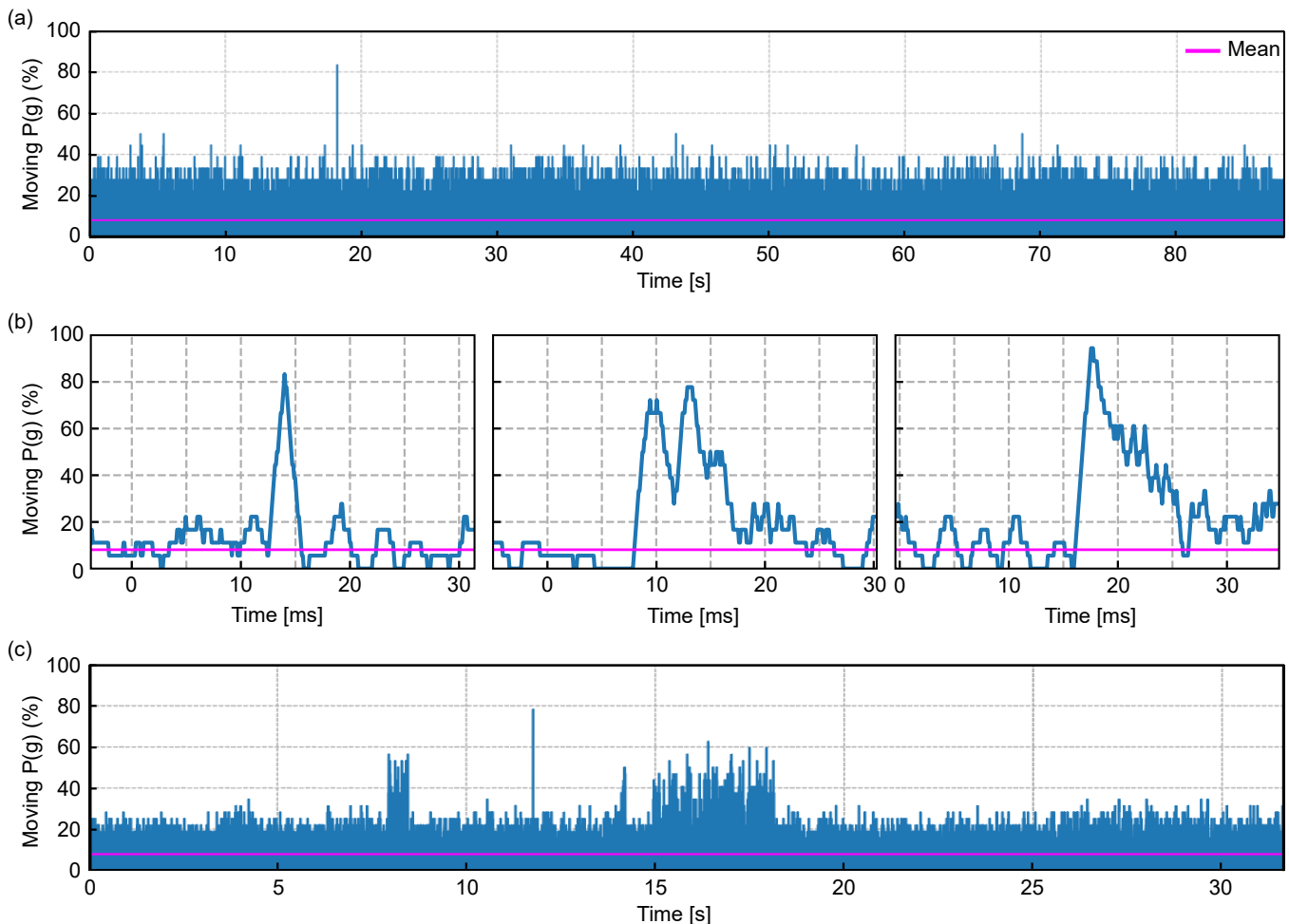


FIG. 3. **Typical signal traces and occasional instability.** (a) An 88 second long trace is showing a single spike corresponding to a drastic drop in T_1 . (b) Three different pulse shapes are shown. All such pulses start with a fast rise. (c) The qubits sporadically undergo periods of instability lasting for up to a minute visible in a small fraction of data acquired.

III. PULSE RECONSTRUCTION

For the event detection, we developed an approach based on the probability of observing a certain stream of $|e\rangle$ and $|g\rangle$. Initially, we performed a simultaneous Gaussian fit to the distribution of I/Q of $|g\rangle$, $|e\rangle$, and $|f\rangle$ to correct for time instabilities and removed traces in which the qubit turned out to be in the second excited state $|f\rangle$. The clouds corresponding to $|g\rangle$ and $|e\rangle$ are then rotated in order to be aligned along one quadrature and projected onto the other. Further information can be found in the Supplementary Section D.

We then performed a Gaussian fit to determine the point at which $|g\rangle$ and $|e\rangle$ were maximally separated, enabling us to convert the measured I/Q values to a sequence of 0 (for $|g\rangle$) and 1 (for $|e\rangle$). This stream of zeros and ones was further processed to construct pulses for event detection. We started with the assumption that, for each measurement, the probability of the qubit remaining in state $|e\rangle$ is equal to $e^{-\Delta t_d/T_1}$. Since, our readouts took several micro-seconds, we added that to

the waiting period to accurately compute Δt_d . Moreover, we found that the qubit relaxations varied by 25-30% over the data acquisition period (see Fig. 1(b)), consistent with the typical behavior of transmon devices [43]. Therefore, T_1' was computed using 10^6 points (corresponding to approximately one minute worth of data) and used to estimate the probability for the qubit to be in state $|e\rangle$.

We began by picking the first 50 points of the trace and computing the probability P for observing the measured counts of zeros and ones according to the Binomial probability distribution. Subsequently, we moved to the next point of the trace and repeated the calculation. Given that the probability for the qubit to be in state $|e\rangle$ was approximately 85–90%, the probability of observing a large number of zeros in a subsequent series of measurements was very small. Finally, we computed the absolute logarithm ($|\log(P)|$) of this probability, simply to avoid working with very small numbers. If the probability of observing this series of events was smaller than 1% ($|\log(P)| > 4.6$), the software trigger was fired, and

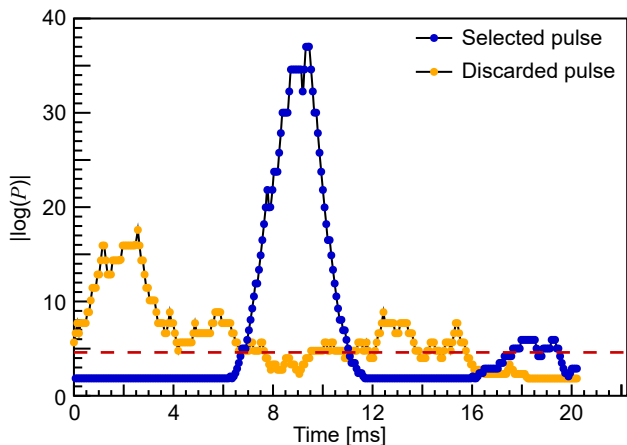


FIG. 4. **Examples of triggered pulses.** The orange trace shows a discarded pulse as the acquisition window starts with the tail of a preceding event. A selected pulse is shown in blue where the baseline region is clean. The red dashed line indicates the software trigger threshold.

we saved a pulse with a length of 450 points, 100 of which were acquired before the pulse to monitor the status of the qubit before the interaction. Typical triggered pulses are shown in Fig. 4.

We then computed several quantities to characterize each pulse, including the value of the maximum, the length (defined as the number of points above threshold), the position of the maximum, as well as the value and root-mean-square (RMS) of the baseline before the pulse. These parameters were used to discard non-physical pulses (see orange trace in Fig. 4), such as those occurring on the tail of a preceding pulse or with a maximum too far from the trigger position. Consistency in data selection was ensured by applying the same criteria across all runs.

IV. RESULTS AND DISCUSSION

The histogram of $\text{Max}(|\log(P)|)$ of the selected pulses is shown in Fig. 5. The single qubit measured in the fully shielded facility at LNGS features a rate of $(23 \pm 4) \times 10^{-3}$ events/sec (solid gray trace). This is obtained by using the measurement time of 28 min, which is selected to filter periods with some unwanted excitation of the $|f\rangle$ state. This shorter time causes larger statistical uncertainty. We repeated the analysis including longer intervals (in which $|f\rangle$ state was sometimes excited) in order to increase the statistics and obtained $(10 \pm 1) \times 10^{-3}$ events/sec (hatched gray trace). This factor two discrepancy can be considered as the systematic uncertainty on the result. The observed background event rate is about 2.5 to 5 times higher than the predicted rate from simulations, which is $(4.0 \pm 0.6) \times 10^{-3}$ events/sec. This discrepancy suggests the presence of other sources of decoherence that resemble quasiparticle burst events but cannot be ascribed to radioactive sources.

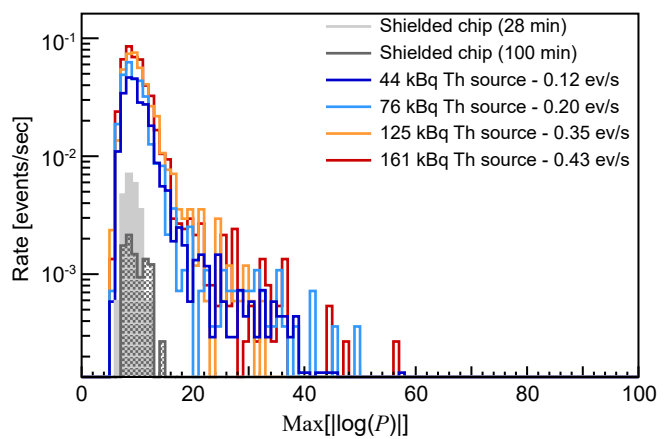


FIG. 5. **Maximum of the selected events.** Gray filled histograms represent the data collected with the chip shielded from the environment (in the deep underground LNGS, where the cryogenic facility is equipped with a ~ 10 cm thick external copper+lead shield and with an internal dual stage lead shield). The dataset (solid gray) corresponding to 28 minutes had all $|f\rangle$ population discarded whereas the longer one (hatched gray) had partial $|f\rangle$ population. Other histograms refer to pulses acquired by exposing the chip to Thorium gamma sources with increasing activity (from 44 to 161 kBq), resulting in an increasing rate of interaction in the chip (from 0.12 to 0.43 events/sec, according to the results of the simulation reported in Table S3 of Supplementary Section C. The histograms are scaled by the length of the run.

Figure 5 clearly demonstrates that exposing the chip to a radioactive source results in an excess of events. The rate of these events increases linearly with the intensity of the source itself. Next, we compare the triggered and simulated rates for the various Thorium sources in Fig. 6.

The slope parameter p_1 of the linear fit in Fig. 6 shows that setting the threshold at 1% probability allows us to reach a detection efficiency of $(68 \pm 8)\%$. This result indicates that qubits are sensitive to laboratory gamma radioactivity, despite the fact that gamma rays deposit a lower amount of energy compared to cosmic rays [22, 33]. This is not a significant concern for the development of quantum processors, as minimal passive shielding around the facility can largely mitigate this radioactive source [39, 50, 51]. Conversely, the absence of a high energy threshold for gamma detection presents interesting opportunities for using qubits as particle detectors [52]. While the primary objective of this work was not to operate a qubit as a particle detector, it is evident that optimizing the threshold or trigger algorithm, along with employing more refined pulse reconstruction algorithms (such as matched filter algorithms), could significantly improve detection efficiency.

However, from the linear fit the intercept p_0 results in (0.17 ± 0.02) events/second. This parameter can be interpreted as the expected rate in the absence of radioactive interactions (if the qubit response to the source is fully linear) and exceeds the one measured in the “back-

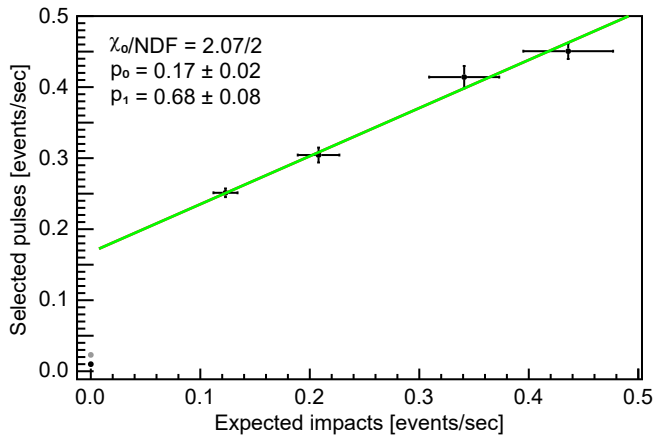


FIG. 6. **Measured rate of events as a function of the rate expected from the simulation.** Data were modelled using a first-degree polynomial. The linear coefficient p_1 can be considered as the detection efficiency. The intercept p_0 represents the expected rate in absence of Thorium sources. The fit was done excluding the two points measured in the “shielded” configuration. Uncertainties on the triggered rates are statistical only, while uncertainties on the expected impacts are dominated by the systematic uncertainties in the simulation.

ground” run. Future work will investigate this discrepancy further.

We deepened the study of the effect of radioactivity by investigating a possible activation of two-level-systems (TLS) when deploying the gamma source. As pointed out in Ref. 23, the ionizing effect of radiation on the chip and the consecutive charge recombination could locally affect the distribution of charges and the electric field that they produce, to which TLSs are sensitive. As a result, the TLSs’ frequencies could shift, getting into resonance or out of resonance with the qubit. This would cause a fluctuation of the qubit T_1 lasting longer than the recombination time of the quasiparticles produced by an impact.

We analyzed the data obtained from the measurements done at LNGS when exposing the qubit to the 161 kBq Thorium source. We selected pulses with very high maxima ($|\log(P)| > 14$), so to discard possible noise events. For each pulse we calculated the average values of $|\log(P)|$ approximately 10 ms before the trigger and tens of milliseconds after it, when the quasiparticle poisoning was already over. A change in the qubit T_1 due to TLS dynamics would result in an average value of $|\log(P)|$ after the pulse different from what obtained before the trigger.

We made the histogram of $\Delta(\log(P))$ for radioactivity impacts and compared it with what obtained by selecting noise events instead (Fig. 7). We didn’t observe significant differences between the two histograms. To double check this result we exposed our qubit to a Cesium source which activity was an order of magnitude higher than the Th source one. Also in that case, no significant

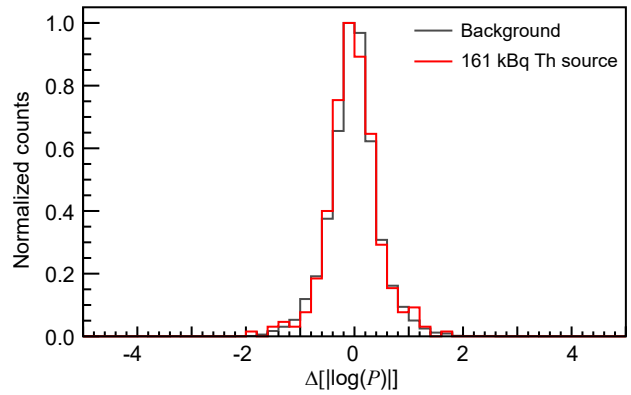


FIG. 7. **Fluctuations in the value of $\log(P)$.** Fluctuations were computed for pulses detected in the case of no sources (red) and when the qubit was exposed to the 161 kBq Thorium source (gray) at LNGS. Histograms have been normalized in order to have their maximum value equal to 1.

differences between radioactivity events and noise events were observed.

This analysis showed that the fluctuations in the qubit T_1 correlated to radioactivity impacts were of the same magnitude of what caused by other sources of noise. Given also the high rate of noise events that we observed, we concluded that ionizing radiation does not play a major role in undermining the T_1 stability of the qubit we studied.

Finally, we investigated whether radioactive impacts could excite the qubit from $|g\rangle$ to $|e\rangle$ state. To this aim, we performed the same study described above, but with a reversed measurement protocol: initializing the qubit in the state $|g\rangle$ instead of $|e\rangle$, and monitoring the qubit exposed to a strong gamma source. Interestingly, exposing the qubit to gamma radiation did not result in an excess of events as demonstrated in Fig. 10. This observation is consistent with what was previously reported in Ref. 20, confirming that quasiparticles generated due to radiation do not deliver energy to transmon qubits.

Finally, we conducted a similar fast decay protocol study using multiple “twin-chips” operated at the above ground facilities at SQMS Fermilab. Here qubits are fully unshielded from cosmic and gamma radiation. The results showed consistency with those obtained at LNGS, as we obtained qualitatively similar distributions in all the pulse parameters defined for our study. The distribution of $\text{Max}(|\log(P)|)$ in particular, is reported in Figure 8. The histograms do not reveal any distinct behavior of the chip in the measurements conducted deep underground at LNGS compared to those above-ground at FNAL. The protocol applied to three qubits at FNAL under ambient radiation conditions showed varied responses: similar (Q4), reduced (Q2), and increased (Q3) rates when compared to the response of the maximally shielded qubit at LNGS.

These variations observed in the rates for different qubits measured at FNAL compared to the LNGS back-

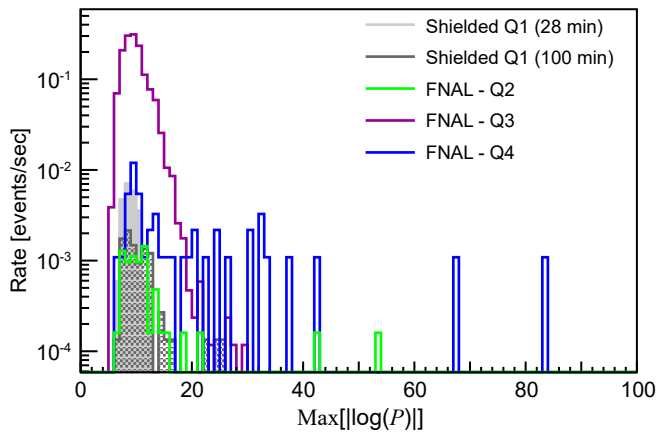


FIG. 8. **Histograms of $\text{Max}[\log(P)]$ for FNAL qubits compared to LNGS background.** Gray filled histograms represent the same data as in Fig. 5. The other histograms refer to data acquired at FNAL using three similar transmon qubits. The histograms do not reveal any distinct behavior of the chip in the measurements conducted deep underground at LNGS compared to those above-ground at FNAL

ground one indicate that modern transmons are dominated by other sources of noise and radiation does not play a major role in the drastic drop in T_1 at short time scales. This fact has also been corroborated by another recent study [41] where cosmic rays are not found to be a strong contributor to the most frequent correlated error (four qubits).

Even though we did not experimentally observe a measurable effect of environmental radiation induced errors, we can utilize the simulated rates to give a cap estimate for the relevant timescales at which radiation would start to affect quantum computation.

The probability to have at least one event in a time window ΔT is given by $P_{\text{impact}} = 1 - e^{-r \cdot \Delta T}$, where r is the rate of impacts. Using the simulated rates, for environmental radioactivity we find that in a non-shielded laboratory setting a quantum computation would be affected by radioactivity less than 0.1% (1%) times if the computation is completed within approx 17 ms (170 ms). Note that the computation may include multiple runs of an algorithm and not necessarily require to be a single run lasting for ΔT . At a fully shielded environment like LNGS, due to much lower expected rate, we have instead $P_{\text{impact}} < 0.1\%$ (1%) if $\Delta T \lesssim 250$ ms (2.5 s). The available computation period increases if higher error probability is tolerated. Figure 9 shows available computational time as a function of radiation impact rates around values estimated for the two cases. The contour lines show various constant error rates and the horizontal green shaded area (< 1 ms) represents the T_1 times of contemporary transmon qubits. In this regime, radiation causes error with a minuscule $P_{\text{impact}} < 10^{-4}$. In other words, when a calculation is repeated $> 10^4$ times, one result will be corrupted due to radiation. Most of the modern algorithms running on quantum hardware

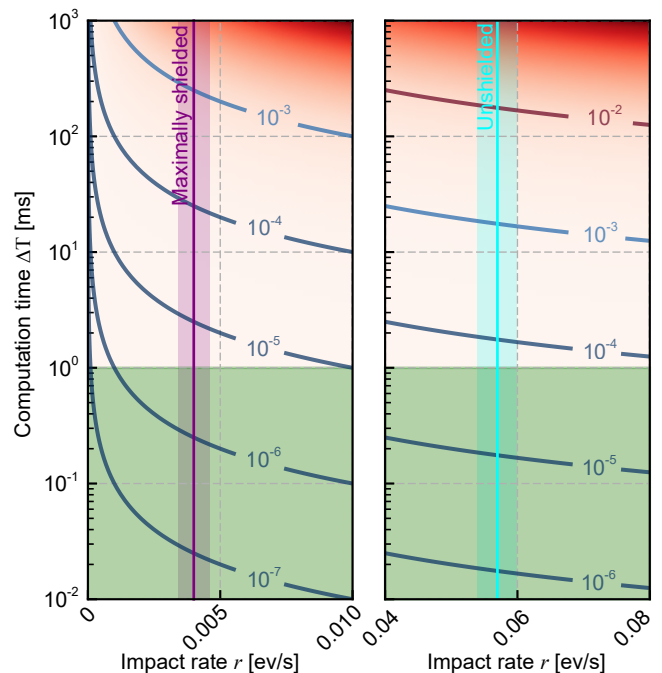


FIG. 9. **Relationship between available computational time and radiation rate for different error probability tolerance.** The contours show fixed error probability lines as a function of available computational time ΔT and the rate of impacts r . The purple (cyan) vertical line with shaded area show the simulated rate for maximally shielded (LNGS) versus non-shielded. The horizontal green area ($\Delta T < 1$ ms) highlight the lifetimes of modern transmon qubits. The error rates in this regime is less than 10^{-4} making radiation an insignificant contributor.

like variational quantum eigensolver or quantum approximate optimization take less than a milli-second for a single iteration and require a large number of repetitions ($\sim \mathcal{O}(10^4)$). Therefore, we can safely conclude that radiation has negligible effect on modern transmon-based quantum computing platforms even if error-correction fails due to an impact.

V. CONCLUSIONS

We have performed a comparative study of how radiation may affect transmon qubits hosted at two laboratories with very distinct radiation environments. The regular T_1 experiments performed on the same qubit showed no difference in qubit lifetimes of the order of 100 microseconds. The experiments with controlled Thorium sources conducted at the deep underground Gran Sasso laboratory demonstrate the possibility of achieving a good detection efficiency, opening the possibility of using transmons as a particle detector. However, the background rate observed with no active sources at LNGS show higher event rates compared to the simulated values, indicating that other noise sources produce signa-

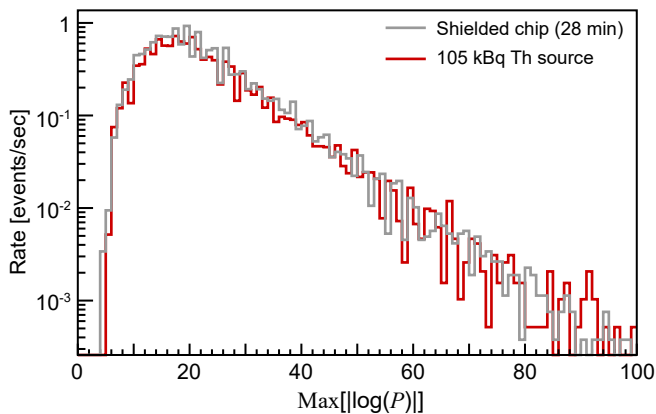


FIG. 10. **Event maxima from the $|g\rangle \rightarrow |e\rangle$ data.** We didn't observe any excess of events when exposing the qubit to the Thorium source.

tures similar to those expected or conjectured to be coming from radiation.

The same protocol when applied to multiple similar qubits in Fermilab (above-ground and with no lead shield) with ambient radiation, shows both increased and reduced rates compared to the response of the maximally shielded qubit at LNGS. These results suggest that these radiation-like events lasting milliseconds are generated by different sources, and that radiation is not a major source of errors in modern transmon qubits. Based on the experimental and simulated results we find that quantum computation will be affected at a maximum of a percent level due to radiation inflicted single-qubit errors when computational time reaches more than 170 ms at fully unshielded facilities and 2.5 s at LNGS. We found no correlation of radiation events to TLS scrambling or qubit excitation.

Future experiments will aim at in-depth understanding of the various error sources which are currently dominating over the radiation induced effects. This will involve further investigations based on fast decay proto-

cols testing different qubit geometries, materials and synchronized measurements across same and different chips. SQMS is focused on enhancing the T_1 of transmon qubits and so future measurements will investigate the behavior of qubits with a wide distribution of coherence performance ranging from tens of microseconds to approaching milliseconds. Advancing this knowledge will be critical for the use of superconducting qubits for quantum computation and sensing.

ACKNOWLEDGMENTS

The authors thank the Director and technical staff of the Laboratori Nazionali del Gran Sasso. We are also grateful to the LNGS Computing and Network Service for computing resources and support on U-LITE cluster at LNGS. We are grateful to A. Girardi for the controller of the cryogenic switch, M. Guetti for the help with the whole cryogenic facility (including its continuous upgrades), and M. Iannone for the assembly of the device at LNGS. We are thankful to Theodore C. III and Grzegorz Tatkowski for providing support on experimental preparations and cryogenic operations at FNAL. T.R. thanks Xinyuan You for useful discussions.

The work was supported by the U.S. Department of Energy, Office of Science, National Quantum Information Science Research Centers, Superconducting Quantum Materials and Systems (SQMS) Center under the contract No. DE-AC02-07CH11359, by the Italian Ministry of Foreign Affairs and International Cooperation, grant number US23GR09, by the Italian Ministry of Research under the PRIN Contract No. 2020h51338 (“Thin films and radioactivity mitigation to enhance superconducting quantum processors and low temperature particle detectors”) and by the Italian Ministry of Research under the PRIN Contract No. 2022BP4H73 (Chasing Light Dark Matter with Quantum Technologies”).

-
- [1] R. Barends, J. Kelly, A. Megrant, A. Veitia, D. Sank, E. Jeffrey, T. C. White, J. Mutus, A. G. Fowler, B. Campbell, Y. Chen, Z. Chen, B. Chiaro, A. Dunsworth, C. Neill, P. O'Malley, P. Roushan, A. Vainsencher, J. Wenner, A. N. Korotkov, A. N. Cleland, and J. M. Martinis, Superconducting quantum circuits at the surface code threshold for fault tolerance, *Nature* **508**, 500 (2014).
 - [2] F. Arute *et al.*, Quantum supremacy using a programmable superconducting processor, *Nature* **574**, 505 (2019).
 - [3] M. Kjaergaard, M. E. Schwartz, J. Braumüller, P. Krantz, J. I.-J. Wang, S. Gustavsson, and W. D. Oliver, Superconducting qubits: Current state of play, *Annual Review of Condensed Matter Physics* **11**, 369 (2020).
 - [4] Rigetti aspen-m-2 features, <https://www.rigetti.com/what-we-build>.
 - [5] Y. Wu, W.-S. Bao, S. Cao, F. Chen, M.-C. Chen, X. Chen, T.-H. Chung, H. Deng, Y. Du, D. Fan, M. Gong, C. Guo, C. Guo, S. Guo, L. Han, L. Hong, H.-L. Huang, Y.-H. Huo, L. Li, N. Li, S. Li, Y. Li, F. Liang, C. Lin, J. Lin, H. Qian, D. Qiao, H. Rong, H. Su, L. Sun, L. Wang, S. Wang, D. Wu, Y. Xu, K. Yan, W. Yang, Y. Yang, Y. Ye, J. Yin, C. Ying, J. Yu, C. Zha, C. Zhang, H. Zhang, K. Zhang, Y. Zhang, H. Zhao, Y. Zhao, L. Zhou, Q. Zhu, C.-Y. Lu, C.-Z. Peng, X. Zhu, and J.-W. Pan, Strong quantum computational advantage using a superconducting quantum processor, *Phys. Rev. Lett.* **127**, 180501 (2021).
 - [6] J. Chow *et al.*, Ibm quantum breaks the 100-qubit processor barrier (2021), [https](https://arxiv.org/abs/2109.12647) :

- [//research.ibm.com/blog/127-qubit-quantum-processor-eagle](https://research.ibm.com/blog/127-qubit-quantum-processor-eagle).
- [7] A. V. Dixit, S. Chakram, K. He, A. Agrawal, R. K. Naik, D. I. Schuster, and A. Chou, Searching for dark matter with a superconducting qubit, *Phys. Rev. Lett.* **126**, 141302 (2021).
 - [8] A. Agrawal, A. V. Dixit, T. Roy, S. Chakram, K. He, R. K. Naik, D. I. Schuster, and A. Chou, Stimulated emission of signal photons from dark matter waves, *Phys. Rev. Lett.* **132**, 140801 (2024).
 - [9] P. K. Day, H. G. LeDuc, B. A. Mazin, A. Vayonakis, and J. Zmuidzinas, A broadband superconducting detector suitable for use in large arrays, *Nature* **425**, 817 (2003).
 - [10] K. D. Irwin, An application of electrothermal feedback for high resolution cryogenic particle detection, *Applied Physics Letters* **66**, 1998 (1995).
 - [11] J. N. Ullom and D. A. Bennett, Review of superconducting transition-edge sensors for x-ray and gamma-ray spectroscopy, *Superconductor Science and Technology* **28**, 084003 (2015).
 - [12] I. Charaev, D. A. Bandurin, A. T. Bollinger, I. Y. Phinney, I. Drozdov, M. Colangelo, B. A. Butters, T. Taniguchi, K. Watanabe, X. He, O. Medeiros, I. Božović, P. Jarillo-Herrero, and K. K. Berggren, Single-photon detection using high-temperature superconductors, *Nature Nanotechnology* **18**, 343 (2023).
 - [13] L. Cardani, N. Casali, A. Cruciani, H. le Sueur, M. Martinez, F. Bellini, M. Calvo, M. G. Castellano, I. Colantoni, C. Cosmelli, A. D'Addabbo, S. D. Domizio, J. Goupy, L. Minutolo, A. Monfardini, and M. Vignati, Al/ti/al phonon-mediated kIDs for uv-vis light detection over large areas, *Superconductor Science and Technology* **31**, 075002 (2018).
 - [14] A. Cruciani, L. Bandiera, M. Calvo, N. Casali, I. Colantoni, G. Del Castello, M. del Gallo Roccagiovine, D. Delicato, M. Giammei, V. Guidi, J. Goupy, V. Pettinacci, G. Pettinari, M. Romagnoni, M. Tamisari, A. Mazzolari, A. Monfardini, and M. Vignati, BULLKID: Monolithic array of particle absorbers sensed by kinetic inductance detectors, *Applied Physics Letters* **121**, 213504 (2022).
 - [15] B. A. Mazin, B. Bumble, S. R. Meeker, K. O'Brien, S. McHugh, and E. Langman, A superconducting focal plane array for ultraviolet, optical, and near-infrared astrophysics, *Opt. Express* **20**, 1503 (2012).
 - [16] A. Monfardini, A. Benoit, A. Bideaud, L. Swenson, A. Cruciani, P. Camus, C. Hoffmann, F. X. Désert, S. Doyle, P. Ade, P. Mauskopf, C. Tucker, M. Roesch, S. Leclercq, K. F. Schuster, A. Endo, A. Baryshev, J. J. A. Baselmans, L. Ferrari, S. J. C. Yates, O. Bourrion, J. Macias-Perez, C. Vescovi, M. Calvo, and C. Giordano, A dual-band millimeter-wave kinetic inductance camera for the iram 30 m telescope, *The Astrophysical Journal Supplement Series* **194**, 24 (2011).
 - [17] L. Cardani, N. Casali, G. Catelani, T. Charpentier, M. Clemenza, I. Colantoni, A. Cruciani, L. Gironi, L. Gruenhaupt, D. Gusenkova, *et al.*, Demetra: Suppression of the relaxation induced by radioactivity in superconducting qubits, *Journal of Low Temperature Physics* **199**, 475 (2020).
 - [18] M. McEwen, K. C. Miao, J. Atalaya, A. Bilmes, A. Crook, J. Bovaird, J. M. Kreikebaum, N. Zobrist, E. Jeffrey, B. Ying, *et al.*, Resisting high-energy impact events through gap engineering in superconducting qubit arrays, arXiv preprint arXiv:2402.15644 (2024).
 - [19] A. P. Vepsäläinen *et al.*, Impact of ionizing radiation on superconducting qubit coherence, *Nature* **584**, 551 (2020).
 - [20] M. McEwen *et al.*, Resolving catastrophic error bursts from cosmic rays in large arrays of superconducting qubits, *Nature Physics* **18**, 107 (2021).
 - [21] X.-G. Li, J.-H. Wang, Y.-Y. Jiang, G.-M. Xue, X.-X. Cai, J. Zhou, M. Gong, Z.-F. Liu, S.-Y. Zheng, D.-K. Ma, *et al.*, Direct evidence for cosmic-ray-induced correlated errors in superconducting qubit array, arXiv preprint arXiv:2402.04245 (2024).
 - [22] C. D. Wilen *et al.*, Correlated charge noise and relaxation errors in superconducting qubits, *Nature* **594**, 369 (2021).
 - [23] T. Thorbeck *et al.*, TIs dynamics in a superconducting qubit due to background ionizing radiation (2022), arXiv:2210.04780.
 - [24] P. V. Klimov *et al.*, Fluctuations of energy-relaxation times in superconducting qubits, *Phys. Rev. Lett.* **121**, 090502 (2018).
 - [25] S. E. de Graaf *et al.*, Direct identification of dilute surface spins on al₂o₃: Origin of flux noise in quantum circuits, *Phys. Rev. Lett.* **118**, 057703 (2017).
 - [26] J. Burnett *et al.*, Evidence for interacting two-level systems from the 1/f noise of a superconducting resonator, *Nature Communications* **5**, 4119 (2014).
 - [27] A. Bilmes *et al.*, Resolving the positions of defects in superconducting quantum bits, *Scientific Reports* **10**, 3090 (2020).
 - [28] J. Lisenfeld *et al.*, Electric field spectroscopy of material defects in transmon qubits, *npj Quantum Information* **5**, 105 (2019).
 - [29] J. M. Martinis *et al.*, Decoherence in josephson qubits from dielectric loss, *Phys. Rev. Lett.* **95**, 210503 (2005).
 - [30] C. Müller *et al.*, Towards understanding two-level systems in amorphous solids: insights from quantum circuits, *Reports on Progress in Physics* **82**, 124501 (2019).
 - [31] C. R. H. McRae *et al.*, Materials loss measurements using superconducting microwave resonators, *Review of Scientific Instruments* **91**, 091101 (2020).
 - [32] D. Gusenkova *et al.*, Operating in a deep underground facility improves the locking of gradiometric fluxonium qubits at the sweet spots, *Applied Physics Letters* **120**, 054001 (2022).
 - [33] L. Cardani *et al.*, Reducing the impact of radioactivity on quantum circuits in a deep-underground facility, *Nature Communications* **12**, 10.1038/s41467-021-23032-z (2021).
 - [34] F. Henriques *et al.*, Phonon traps reduce the quasiparticle density in superconducting circuits, *Applied Physics Letters* **115**, 212601 (2019).
 - [35] J. M. Martinis, Saving superconducting quantum processors from decay and correlated errors generated by gamma and cosmic rays, *npj Quantum Information* **7**, 90 (2021).
 - [36] V. Iaiia, J. Ku, A. Ballard, C. P. Larson, E. Yelton, C. H. Liu, S. Patel, R. McDermott, and B. L. T. Plourde, Phonon downconversion to suppress correlated errors in superconducting qubits, *Nature Communications* **13**, 6425 (2022).
 - [37] D. T. Le *et al.*, Operating a passive on-chip superconducting circulator: Device control and quasiparticle effects, *Phys. Rev. Research* **3**, 043211 (2021).
 - [38] I. J. Arnquist, M. L. di Vacri, N. Rocco, R. Saldanha, T. Schlieder, R. Patel, J. Patil, M. Perez, and H. Uka,

- Ultra-low radioactivity flexible printed cables, *EPJ Techniques and Instrumentation* **10**, 17 (2023).
- [39] L. Cardani, I. Colantoni, A. Cruciani, F. De Dominicis, G. D’Imperio, M. Laubenstein, A. Mariani, L. Pagnanini, S. Pirro, C. Tomei, N. Casali, F. Ferroni, D. Frolov, L. Gironi, A. Grassellino, M. Junker, C. Kopas, E. Lachman, C. R. H. McRae, J. Mutus, M. Nastasi, D. P. Pappas, R. Pilipenko, M. Sisti, V. Pettinacci, A. Romanenko, D. Van Zanten, M. Vignati, J. D. Withrow, and N. Z. Zhelev, Disentangling the sources of ionizing radiation in superconducting qubits, *The European Physical Journal C* **83**, 94 (2023).
- [40] J. L. Orrell and B. Loer, Sensor-assisted fault mitigation in quantum computation, *Phys. Rev. Applied* **16**, 024025 (2021).
- [41] P. M. Harrington, M. Li, M. Hays, W. V. D. Pontseele, D. Mayer, H. D. Pinckney, F. Contipelli, M. Gingras, B. M. Niedzielski, H. Stickler, J. L. Yoder, M. E. Schwartz, J. A. Grover, K. Serniak, W. D. Oliver, and J. A. Formaggio, Synchronous detection of cosmic rays and correlated errors in superconducting qubit arrays (2024), [arXiv:2402.03208 \[quant-ph\]](https://arxiv.org/abs/2402.03208).
- [42] A. Mariani *et al.*, Mitigation of cosmic rays-induced errors in superconducting quantum processors, *IEEE-QCE23 proceedings* (2023).
- [43] M. Bal, A. A. Murthy, S. Zhu, F. Crisa, X. You, Z. Huang, T. Roy, J. Lee, D. van Zanten, R. Pilipenko, I. Nekrashevich, D. Bafia, Y. Krasnikova, C. J. Kopas, E. O. Lachman, D. Miller, J. Y. Mutus, M. J. Reagor, H. Cansizoglu, J. Marshall, D. P. Pappas, K. Vu, K. Yadavalli, J.-S. Oh, L. Zhou, M. J. Kramer, F. Q. Lecocq, D. P. Goronzy, C. G. Torres-Castanedo, G. Pritchard, V. P. Dravid, J. M. Rondinelli, M. J. Bedzyk, M. C. Hersam, J. Zasadzinski, J. Koch, J. A. Sauls, A. Romanenko, and A. Grassellino, Systematic improvements in transmon qubit coherence enabled by niobium surface encapsulation, *npj Quantum Information* **10**, 43 (2024).
- [44] E. Yelton, C. P. Larson, V. Iaia, K. Dodge, G. L. Magna, P. G. Baity, I. V. Pechenezhskiy, R. McDermott, N. Kurinsky, G. Catelani, and B. L. T. Plourde, Modeling phonon-mediated quasiparticle poisoning in superconducting qubit arrays (2024), [arXiv:2402.15471 \[quant-ph\]](https://arxiv.org/abs/2402.15471).
- [45] M. Martinez, L. Cardani, N. Casali, A. Cruciani, G. Pettinari, and M. Vignati, Measurements and simulations of athermal phonon transmission from silicon absorbers to aluminum sensors, *Phys. Rev. Appl.* **11**, 064025 (2019).
- [46] S. Agostinelli *et al.*, GEANT4—a simulation toolkit, *Nucl. Instrum. Methods. Phys. Res. A* **506**, 250 (2003).
- [47] J. M. Martinis, M. Ansmann, and J. Aumentado, Energy decay in superconducting josephson-junction qubits from nonequilibrium quasiparticle excitations, *Phys. Rev. Lett.* **103**, 097002 (2009).
- [48] M. Lenander, H. Wang, R. C. Bialczak, E. Lucero, M. Mariantoni, M. Neeley, A. D. O’Connell, D. Sank, M. Weides, J. Wenner, T. Yamamoto, Y. Yin, J. Zhao, A. N. Cleland, and J. M. Martinis, Measurement of energy decay in superconducting qubits from nonequilibrium quasiparticles, *Phys. Rev. B* **84**, 024501 (2011).
- [49] L. Stefanazzi, K. Treptow, N. Wilcer, C. Stoughton, S. Montella, C. Bradford, G. Cancelo, S. Saxena, H. Arnaldi, S. Sussman, A. Houck, A. Agrawal, H. Zhang, C. Ding, and D. I. Schuster, The qick (quantum instrumentation control kit): Readout and control for qubits and detectors (2022), [arXiv:2110.00557 \[quant-ph\]](https://arxiv.org/abs/2110.00557).
- [50] J. W. Fowler, P. Szypryt, R. Bunker, E. R. Edwards, I. F. Florang, J. Gao, A. Giachero, S. F. Hoogerheide, B. Loer, H. P. Mumm, N. Nakamura, G. C. O’Neil, J. L. Orrell, E. M. Scott, J. Stevens, D. S. Swetz, B. A. VanDevender, M. Vissers, and J. N. Ullom, Spectroscopic measurements and models of energy deposition in the substrate of quantum circuits by natural ionizing radiation (2024), [arXiv:2404.10866](https://arxiv.org/abs/2404.10866).
- [51] B. Loer, P. M. Harrington, B. Archambault, E. Fuller, B. Pierson, I. Arnquist, K. Harouaka, T. D. Schlieder, D. K. Kim, A. J. Melville, B. M. Niedzielski, J. K. Yoder, K. Serniak, W. D. Oliver, J. L. Orrell, R. Bunker, B. A. VanDevender, and M. Warner, Abatement of ionizing radiation for superconducting quantum devices (2024), [arXiv:2403.01032](https://arxiv.org/abs/2403.01032).
- [52] R. Linehan, I. Hernandez, D. J. Temples, S. Q. Dang, D. Baxter, L. Hsu, E. Figueroa-Feliciano, R. Khatiwada, K. Anyang, D. Bowring, G. Bratrud, G. Cancelo, A. Chou, R. Gualtieri, K. Stifter, and S. Sussman, Estimating the energy threshold of phonon-mediated superconducting qubit detectors operated in an energy-relaxation sensing scheme (2024), [arXiv:2404.04423](https://arxiv.org/abs/2404.04423).

Author Contributions

M.B. and F.C. designed and fabricated the transmon devices. S.Z. performed initial characterization of the qubits. A.C. T.R., F.D.D. and D.H. run the experiments. N.C. developed the Bernoulli algorithm. A.M., F.D.D., T.R. and L.C. performed the data analysis. D.V.Z. helped in writing acquisition software. A.M. performed GEANT4 simulations. I.C., A.P., L.P. and S.P. oversaw the cryostat upgrade for the measurements and the cryogenic operations. T.R., A.M., F.D.D., A.G. and L.C. wrote the manuscript with inputs from all the co-authors in interpreting the results. T.R., A.G. and L.C. conceived and supervised the whole project.

SUPPLEMENT

A. Device Fabrication

The devices are fabricated on a $432\ \mu\text{m}$ thick c -plane HEMEX grade double-polished sapphire substrate with 2-inch diameter. The substrate preparation, base-layer (Nb) deposition and Josephson junction evaporation are similar to the fabrication methods followed in Ref. 43. In order to prevent oxidation of the Niobium, a capping layer of thickness $10\ \text{nm}$ is deposited using the same sputtering tool without breaking the vacuum. Gold and Tantalum are used as capping layers for devices Q1 and Q2-Q4 respectively (on two different chips). Device Q1 is first measured at FNAL and then sent to LNGS. The other qubit samples (Q2-Q4) are measured at FNAL. In Table S1, we list the measured parameters of the devices and Fig. S1 shows the relative position of those.

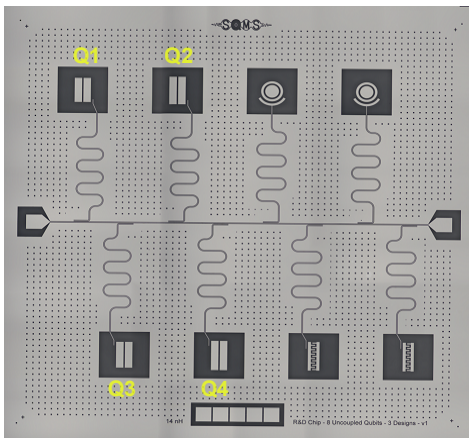


FIG. S1. **Chip layout showing relative position of the transmon qubits.** The other qubits with concentric and inter-digited pads are not used in the experiments due to lower T_1 .

B. Measurement Setup

Our measurement setups at the two locations are shown in Fig. S2. The transmon qubit is measured in the hangar geometry, where a $\lambda/4$ CPW readout resonator is coupled to a transmission line. The pulses for both qubit control and readout are sent through a common input line. The input line is attenuated by 60-70 dB distributed between the 4-K and mixing chamber stages. Copper-body 20 dB attenuators are used at the base plate for better thermalization. At LNGS, the input line is also filtered through a 8 GHz reflective low-pass filter and a strong infrared filter (QMC-CRYOIRF-002) to reduce high-frequency noise. The superconducting output line is protected from the incoming noise through a 4-8 GHz triple junctions isolator, an 8 GHz low-pass filter and a weak infrared filter (QMC-CRYOIRF-001).

At FNAL, both the input and output lines are filtered through 11 GHz reflective low-pass filters. The superconducting output line also has two 4-8 GHz isolators. The device boxes at both locations are protected from stray magnetic fields using cryoperm shields. The output signal is first amplified through a commercial HEMT amplifier at the 4-K plate, followed by a room-temperature amplifier outside the fridge before digitization. The qubit control and readout pulses are generated digitally using a RFSoc ZCU 216 evaluation board and the QICK [49] software.

C. Simulation of Interaction Rates

We use the GEANT4-based Monte Carlo simulation developed in Cardani et al. [39] within the SQMS *Round Robin* project with updated parameters. The aim is to predict both the rate of impacts and the amount of energy released in the Sapphire substrate. The geometry implemented in the simulation, shown in Fig. S3, includes (from outside to inside):

- a. An $80 \times 80\ \text{cm}^2$, 5 cm-thick lead base;
- b. An $80 \times 80\ \text{cm}^2$, 5 cm-thick copper base;
- c. 1/2 round of $10 \times 20\ \text{cm}^2$, 5 cm-thick Pb bricks;
- d. 1 round of $10 \times 20\ \text{cm}^2$, 5 cm-thick Pb bricks;
- e. 1 round of $10 \times 66.5\ \text{cm}^2$, 2 cm-thick Cu bars;
- f. A two layers Permimphy magnetic shielding (Outer layer: $55.6\ \text{cm (OD)} \times 91.3\ \text{cm}$, 1.5 mm-thick; Inner layer: $51\ \text{cm (ID)} \times 89\ \text{cm}$, 1.5 mm-thick);
- g. A $48.1\ \text{cm (OD)} \times 119.5\ \text{cm}$ simplified version of the cryostat with internal vessels;
- h. A CryoPerm® magnetic shield below the mixing chamber;
- j. A 3 cm-thick lead plate at 10 mK, placed between the sample and the electronic components used as internal gammas shield;
- k. A $30.23 \times 30.23 \times 6.3\ \text{mm}^3$ gold-plated copper box hosting the chip.

The chip substrate ($7.5 \times 7.5\ \text{mm}^2$, $432\ \mu\text{m}$ -thick HEMEX Sapphire) is considered the only active volume, where we store tracks and record the energy released by each simulated interaction. The main external contributions, namely environmental gammas and muons, are generated according to the methods described in our previous work [39]. For each source, and for both FNAL and INFN-LNGS laboratories, we estimate the rate of interactions in the chip by scaling the number of recorded events to the flux measurements reported in Section 3 of Ref. [39].

Parameter	Q1	Q2	Q3	Q4	Units
Material	Nb/Au	Nb/Ta	Nb/Ta	Nb/Ta	N/A
Qubit frequency	4717.4	4455.4	4451.3	4294.8	MHz
Readout frequency	7206.8	7055.0	6886.5	6714.5	MHz
Qubit π pulse length	0.150	0.091	0.124	0.160	μ s
Qubit average T_1	84	141	131	214	μ s
Readout pulse length	4.5	3.8	4.0	8.0	μ s
Waiting period	5.0	10.0	5.0	5.0	μ s
Cooldown period	50.0	70.0	70.0	10.0	μ s
One iteration period	64.550	87.929	84.324	31.660	μ s

TABLE S1. Parameters of devices used in the experiments.

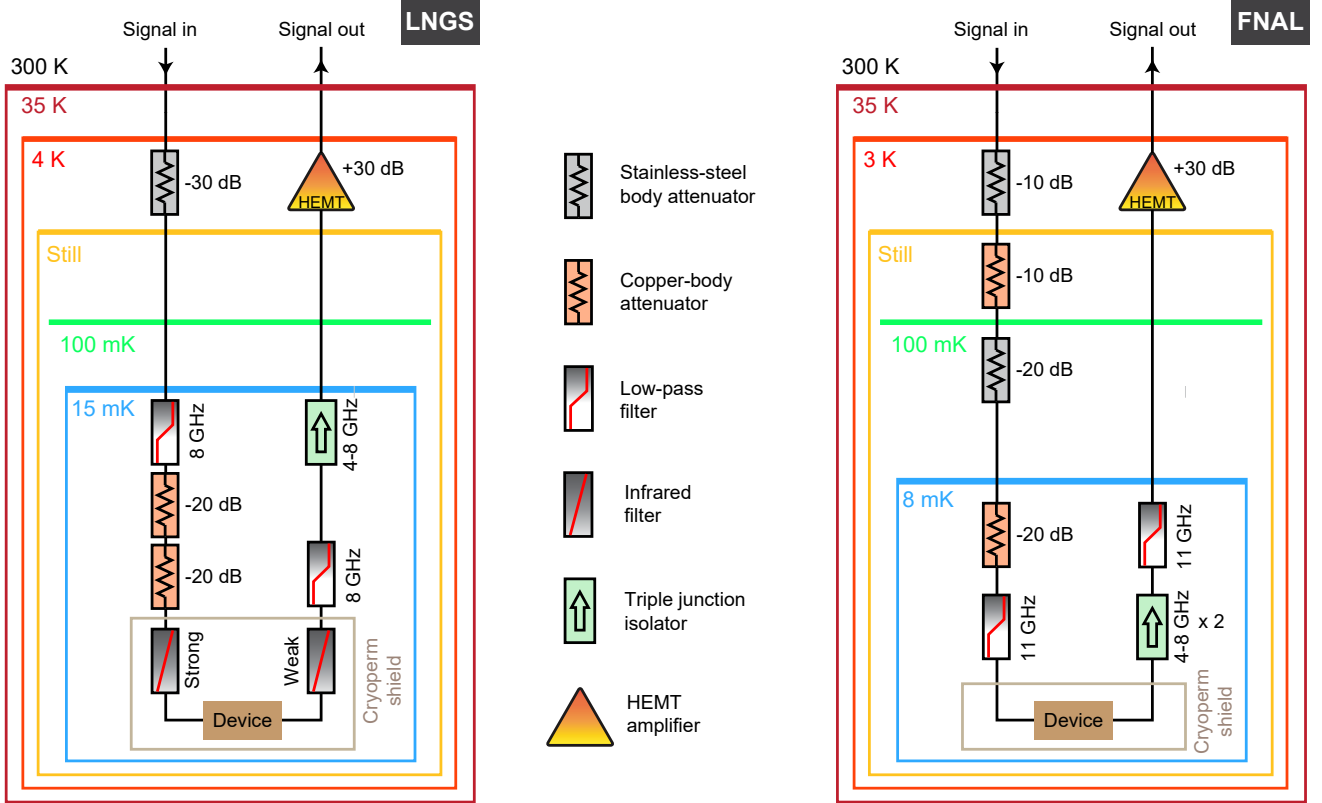


FIG. S2. Cryogenic wiring diagram of the measurement setups at INFN-LNGS and at Fermilab.

Regarding close sources of radioactivity, we simulate the radioactive decays of relevant isotopes (^{40}K , ^{232}Th and ^{238}U chains) uniformly distributed within the volume of the two Printed Circuit Boards (RO4003C produced by ROGERS Corporation) located at the opposite ends of the qubit chip. PCBs indeed constitute the only significant contribution from close sources, as detailed in [39]. We then estimate the rate of interactions in the chip by scaling the number of recorded events to the activities reported in Table S2. These activities are determined by converting the concentrations measured using Inductively Coupled Plasma Mass Spectrometry (ICP-MS) at the Chemistry facility in INFN-LNGS.

Source	^{40}K	^{232}Th	^{238}U
	[mBq/kg]	[mBq/kg]	[mBq/kg]
PCB	(518.8 ± 259.4)	(164.0 ± 41.0)	(161.2 ± 49.6)

TABLE S2. Activities of the relevant radioactive isotopes in the RO4003C PCBs produced by ROGERS Corporation. These values were determined by converting the corresponding concentration measured by ICP-MS at the Chemistry facility at INFN-LNGS.

Figure S4 presents the results of the Monte Carlo simulation, showing the rate of events as a function of the

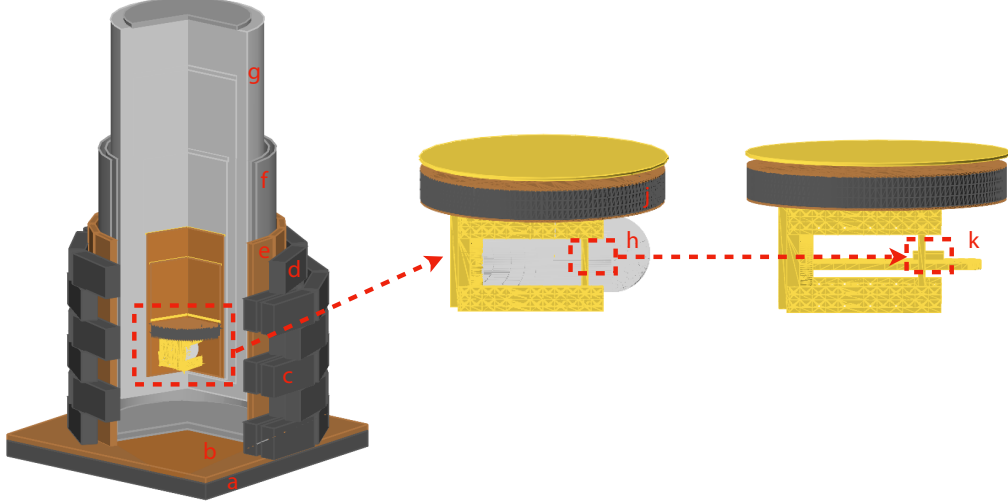


FIG. S3. **Experimental setup of LNGS as implemented in the simulation.** a-e) External gamma shield; f) External two-layer Perminphy magnetic shield; g) Cryostat with internal vessels; h) Internal CryoPerm[®] magnetic shield; j) Internal gamma shield; k) Gold-plated copper box hosting the chip. The full description of the components is reported in the text.

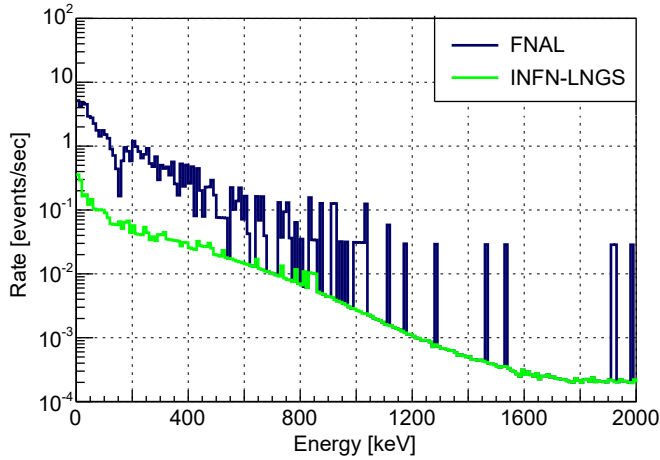


FIG. S4. **Rate of interactions expected in the Sapphire chip as a function of the energy deposited in the chip itself.** The results are shown for both FNAL (blue) and INFN-LNGS (green). In the FNAL case, the total rate is dominated by environmental gammas ($\sim 4.6 \times 10^{-2}$ events/sec), while in the INFN-LNGS scenario the primary contribution comes from radioactive decays in the PCBs ($\sim 2.7 \times 10^{-3}$ events/sec).

energy deposited in the qubit substrate for both FNAL and INFN-LNGS facilities. The event rates for each radiation source are reported in Table I. Notably, the overall rate is expected to be approximately an order of magnitude lower at INFN-LNGS (4×10^{-3} @INFN-LNGS vs. 57×10^{-3} @FNAL), where the dominant contribution is from the PCBs.

To investigate the rate in the presence of the Thorium radioactive sources used at INFN-LNGS, we generate radioactive decays from a point-like ^{232}Th radioactive

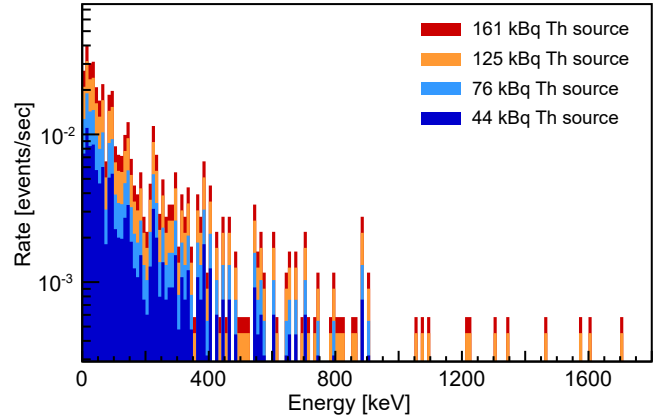


FIG. S5. **Rate of interactions expected in the Sapphire chip as a function of the energy deposited in the chip when exposed to Thorium radioactive sources.** The distinct colors in the plot correspond to the various activities used in the measurements.

source positioned between the external magnetic shield and the copper bars, approximately at the same height of the chip. For this simulation, we consider only gamma emitters in the chain (^{228}Ra , ^{228}Ac , ^{212}Pb , ^{212}Bi and ^{208}Tl), since α and β particles cannot reach the chip as they are shielded by the cryostat. As in the previous case, we determine the rate of interactions in the chip by scaling the number of recorded events to the activities reported in Table S3, which correspond to the Thorium source activities employed in the measurements. The rate of events in the chip, plotted as a function of the deposited energy for the various activities, is illustrated in Fig. S3.

Activity [kBq]	Rate [events/sec]
44.2	0.12 ± 0.01
75.9	0.20 ± 0.02
125.4	0.34 ± 0.03
161.0	0.43 ± 0.04

TABLE S3. **Rate of interactions in the Sapphire substrate predicted by the Monte Carlo simulation for different activities of the Thorium sources.** The values used to scale the Monte Carlo simulation correspond to the Thorium source activities employed in the measurements.

D. Qubit State Discrimination

The I/Q values (in-phase and quadrature-phase signals) obtained for each measurement depend on the state of the qubit. When a large counts of measurements are plotted on the I-Q plane, we usually observe two blobs corresponding to $|g\rangle$ and $|e\rangle$. However, we sometimes observe signals corresponding the transmon being in the second excited state $|f\rangle$ as shown in Fig. S6 and we discard those measurements in the analysis.

The blobs corresponding to $|g\rangle$ and $|e\rangle$ are rotated in order to have the centers at the same value of Q and projected onto the I axis. In this way it is possible to discriminate between the two states by putting a threshold value only on one (I) quadrature.

The populations of the states have been estimated by doing a simultaneous fit on the two quadratures with the RooFit toolkit. The fit function used was a sum of 2D gaussians, one for each blob we were observing. The data was divided into traces of approx. 1 minute duration, and for each of them the simultaneous fit was performed. In this way we were able to identify periods in which the qubit was showing a high population of the $|f\rangle$ state and reject them.

E. Data Analysis

In our analysis we selected events where the probability P of observing a certain number of zeros and ones, calculated according to the Binomial distribution, was below a predefined threshold. Specifically, if the probability of observing such a series of zeros and ones fell below 1%, corresponding to an absolute logarithm ($|\log(P)|$) greater than 4.6, the software trigger was fired, indicating the presence of a potential signal. Once triggered, these data were recorded for further analysis.

By selecting pulses with $|\log(P)| > 4.6$, we observe a trigger rate of 5–6 events/second in the runs performed with the radioactive sources, significantly higher than the expected rate from radioactivity (0.1–0.4 events per second depending on the source activity), suggesting that the majority of triggers are due to noise. To address this, we computed additional variables to refine our data

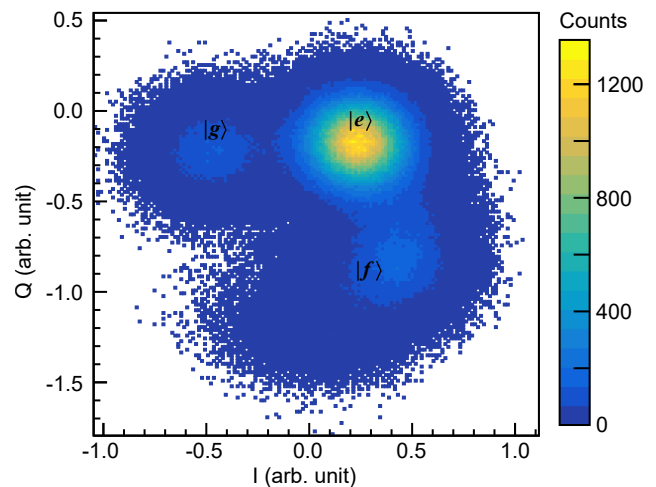


FIG. S6. **Clouds on the I-Q plane corresponding to the qubit states for a subset of the data.** It is possible to observe the cloud corresponding to $|g\rangle$ (left), the cloud corresponding to $|e\rangle$ (upper right) and the cloud corresponding to $|f\rangle$ (bottom right).

selection. Specifically, we calculated:

1. The value and RMS of the baseline before the pulse;
2. The maximum value of $|\log(P)|$;
3. The pulse length, defined as the number of points above threshold;
4. The position of the maximum.

The baseline and its RMS were computed using the first 100 points preceding the trigger. We then removed pulses occurring on the tail of a preceding pulse or those with a “noisy” baseline (see Fig. 4) by requiring a baseline value lower or equal to its mean value $+ 3\sigma$. Additionally, we ensured that the position of the maximum was close to the trigger to avoid re-triggering of the same pulse. Since radioactivity typically results in long pulses (at least 1 ms), we further refined our selection by choosing pulses with length greater than 50 points, corresponding to approximately 3.5 ms under our data-taking conditions.

Finally, we conducted a study to assess the suitability of the window size used for computing the Binomial probability. Our initial choice of 50 points stemmed from the analysis of typical events detected in calibration runs. By averaging tens of these events, we determined that the qubit returned to equilibrium with a characteristic time constant (τ) of 0.78 ms. To ensure complete recovery of the qubit, we adopted a window size corresponding to 5τ , or approximately 4 ms, which translates to 56 points given our sampling frequency of about 0.07 ms^{-1} . We subsequently performed the analysis using window sizes of 20, 30, 70, and 90 points. Our findings confirmed that, for all these window sizes, the detection efficiency could not reach values above 70%. Indeed, when the window size is too small, only a fraction of the signal

can be captured within the window. Conversely, if the window size exceeds the signal length, the number of ze-

ros associated with random qubit de-excitation becomes significant, thus deteriorating the signal-to-noise ratio.